DC-driven subatmospheric glow discharges in the infrared-stimulated

Erhan ONGUN[1], Hatice Hilal YÜCEL (KURT)[1,*], and Selçuk UTAŞ[1]

[1] Department of Physics, Gazi University, 06500, Ankara, Türkiye

ABSTRACT

This paper presents a conceptual framework for experimental research combined with numerical analysis on direct current (DC) glow discharges in microscale planar gas discharge-semiconductor systems (GDSS). In the experimental section, several structural and elemental analyses, including SEM, EDAX, AFM, and near-infrared absorption spectra measurements were carried out for compound semiconductor zinc selenide (ZnSe) cathode sample. Argon (Ar) was charged into the plasma reactor cell of GDSS at pressures of 100 Torr subatmospheric and 760 Torr atmospheric, respectively, by a vacuum pump- gas filling station. Glow discharge light emissions from plasma, excited under three different intensity levels (dark, weak, strong) of infrared beam illumination on ZnSe cathode electrode, were measured by using a phomultiplier tube that is sensitive to UV–Visible wavelengths. In the numerical analysis section, simulation studies were carried out on the two-dimensional gas discharge-semiconductor microplasma system (GDSμPS) cell models using the finite-element method (FEM) solver COMSOL Multiphysics DC plasma program. Calculations and predictions were based on mixture-averaged diffusion drift theory and Maxwellian electron energy distribution function. GDSμPS cell was modeled in a square chamber with planar anode/cathode electrode pair coupled at a 50 μm discharge gap. Single side of ZnSe cathode was finely micro-digitated to increase the effective surface area for enhanced electron emission to the gas discharge cell. The electrical equivalent circuit (EEC) of the proposed model was driven by 1.0 kV DC voltage source. Binary Ar/H_2 gas medium in a mixture of 3:2 molar ratio was introduced to the gas discharge chamber at constant 200 Torr subatmospheric pressure. Simulations were run for normal glow discharges to exhibit the electrical fast transient glow discharge behaviours from electron field emission state to self-sustained normal

Address correspondence to E-mail: hkurt@gazi.edu.tr

E-mail Addresses: erhan.ongun1@gazi.edu.tr; selcuk.utas@gmail.com

🍂 Springer

glow discharge state by numerically solving the electron density (ED), electron current density (ECD) and electric potential distribution (EPD) parameters.

It is figured out that binary Ar/H$_2$ gas discharge model can undertake a major role in shaping and controlling the spatiotemporal response to transient electro-optical behavior of microplasma-based artificial electromagnetic materials configured for high-efficiency infrared-to-visible wavelength conversion applications.

1 Introduction

Several theoretical and experimental research studies have been reported in various areas of plasma science and engineering applications [1–10], including microplasma reactors for ultraviolet (UV) light sources and sensors [11], and gas discharge-semiconductor microplasma systems for infrared (IR) sensors and thermal image converters [12–22].

Various alternative materials have been studied to support the continued development of infrared (IR) detector technology [23, 24]. The major infrared spectral bands are defined as shortwave infrared (SWIR) for wavelengths in the 1–3 μm range, medium-wave infrared (MWIR) for wavelengths in the 3–5 μm range and longwave infrared (LWIR) for wavelengths in the 8–14 μm range [25], and are used depending on the IR sensing and imaging application. Indirect and narrow bandgap semiconductors, including silicon (Si), require integrated cooling equipment to operate as a high-efficiency IR detector.

Group II–VI compound semiconductors can provide optimal response in the multispectral IR range for demanding infrared sensing and imaging applications. Uncooled infrared detectors are largely used in a variety of cost-effective mobile thermal imaging applications, such as early fire detection and remote warning, object detection under low illumination for drivers, handheld night vision imagers and security surveillance. Group II–VI compound semiconductors are also being explored for a variety of specific applications, including photovoltaic cells, light-emitting diodes (LEDs), and infrared solid-state laser sources [26–34].
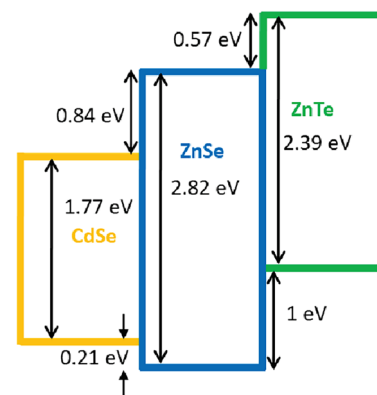
Figure 1 shows a diagram of the valence and conduction band alignments of cadmium selenide (CdSe), zinc selenide (ZnSe) and zinc telluride (ZnTe) compound semiconductors of Group II–VI, which have high intrinsic absorption coefficients [35].

The compound semiconductor zinc selenide (ZnSe) with a direct bandgap of ~ 2.7 eV at 300 K [36–38] has attracted great attention from researchers working in the field of thermal imaging applications [39, 40] due to its fast spectral response in the longwave IR.

A recent study reports on the electrical, optical and structural characterization of ZnSe material for its infrared (IR) sensitivity in the semiconductor-microplasma systems. ZnSe is a preferred material for night-vision devices and infrared windows for its low absorptivity in the infrared spectrum, high transmissivity in the visible spectrum, and high-resolution in the thermal imaging systems in the range of 0.5–15 μm [41].

This conceptual research study experimentally and numerically investigates the direct current -driven glow discharges in microscale planar gas discharge-semiconductor systems (GDSS). Several advanced characterization techniques including, field-emission scanning electron microscopy (FE-SEM), energy dispersive X-ray (EDAX) spectroscopy, high-resolution atomic force microscopy (AFM) were utilized, and absorption spectra measurement data from VIS to NIR were obtained for structural, elemental and optical analyses of the compound semiconductor zinc selenide (ZnSe) sample. Argon was introduced into the gas discharge cell at pressures of 100 Torr and 760 Torr, respectively, using a vacuum-gas filling station. Argon (Ar) was charged into the plasma reactor cell of GDSS at pressures of 100 Torr subatmospheric and 760 Torr atmospheric, respectively, by a vacuum

Fig. 1 Diagram of the valence and conduction band alignments of CdSe, ZnSe and ZnTe [35]

pump- gas filling station. Glow discharge light emissions from plasma, excited under three different intensity levels (dark, weak, strong) of infrared beam illumination on ZnSe cathode electrode, were measured by using a phomultiplier tube.

Numerical analyses were carried out on the two-dimensional gas discharge-semiconductor micro-plasma system (GDSµPS) cell models using the finite-element method (FEM) solver COMSOL Multiphysics DC plasma program based on mixture-averaged diffusion drift theory and Maxwellian electron energy distribution function. A square chamber with planar anode/cathode electrode pair was modeled at 50 µm discharge gap. Single side of ZnSe cathode was finely micro-digitated to increase the effective surface area for enhanced electron emission to the gas discharge cell. The electrical equivalent circuit (EEC) of the proposed model was driven by 1.0 kV DC voltage source. Binary Ar/H_2 gas medium in a mixture of 3:2 molar ratio was introduced to the gas discharge chamber at constant 200 Torr subatmospheric pressure. Simulations were run for normal glow discharges to exhibit the electrical fast transient glow discharge behaviours from electron field emission state to self-sustained normal glow discharge state by numerically solving the electron density (ED), electron current density (ECD) and electric potential distribution (EPD) parameters.

2 Results and discussion

Figure 2 shows a simple sketch of DC -driven planar GDSµPS cell modeled for infrared to visible wavelength conversion application.

Figure 3 introduces the electrical breakdown process in a simple planar anode/cathode -coupled gas discharge medium governed by Townsend electron avalanche reactions through the combination of electron emission and ionization mechanisms [7, 42].

On the sketch in Fig. 3, the indicated abbreviations of TA stands for Townsend electron avalanche multiplication, TE stands for thermionic emission, SEE stands for secondary electron emission, and FE stands for field emission.

SEE coefficient γ_{SE} and TA coefficient α are interlinked by ionizations per unit length and gap distance d, as defined in Eq. 1:
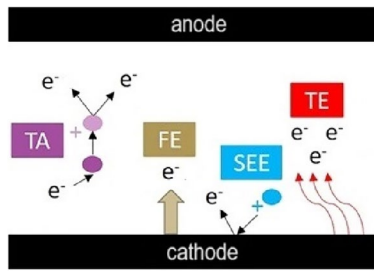
$$\text{Exp}\,(\alpha.d) - 1 = \gamma_{SE}^{-1} \tag{1}$$

Ion-induced secondary electron emission due to the interaction with cathode introduces a contribution of γ' to γ_{SE}, as defined in Eq. 2:

$$\text{Exp}\,(\alpha.d) - 1 = \left(\gamma_{SE} + \gamma\right)^{-1} \tag{2}$$

Fig. 2 Sketch of DC-driven planar GDSµPS cell modeled for infrared to visible wavelength conversion application
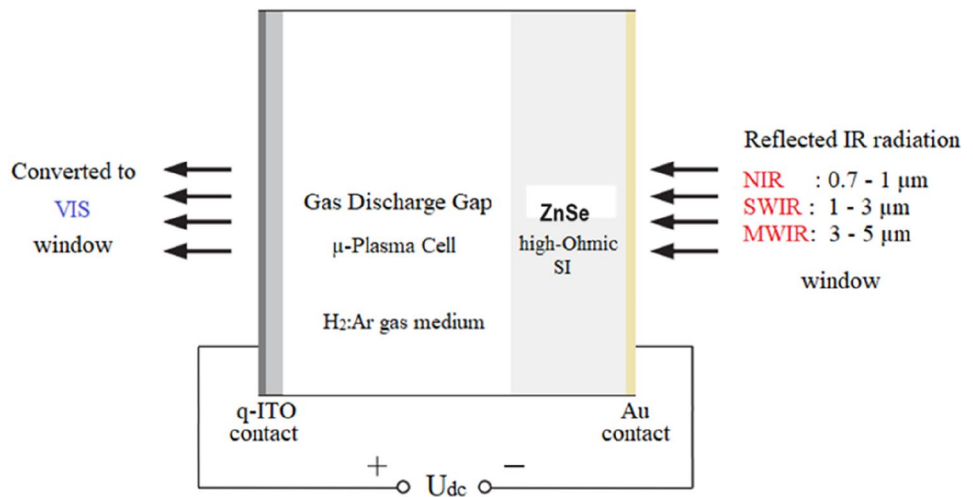
Fig. 3 Electrical breakdown process in a simple planar anode/cathode -coupled gas discharge medium [42, 7]

2.1 Structural and elemental analyses

A sample piece of zinc selenide (ZnSe) cathode wafer was examined to reveal its structural and elemental properties by performing energy dispersive X-ray analysis (EDAX), high-resolution atomic force microscopy (AFM) analysis and field-emission scanning electron microscopy (FE-SEM) analysis. Figure 4 exhibits EDAX data of ZnSe sample with 65.04% Se and 34.96% Zn elements by weight.

Figure 5 shows surface image of ZnSe sample taken at 10,000X magnification by SEM.

Figure 6 shows two and three-dimensional AFM surface images of ZnSe sample with a scan area of 1 μm × 1 μm. The images reveal surface roughness of around 8.0 nm maximum at depth profile.

Figure 7 shows the visible/near-infrared absorption spectra of uncoated ZnSe sample. Near-infrared (NIR) spectral window ranges from 800 nm to 1,500 nm for operation of the proposed GDSμPS cell model by this study.
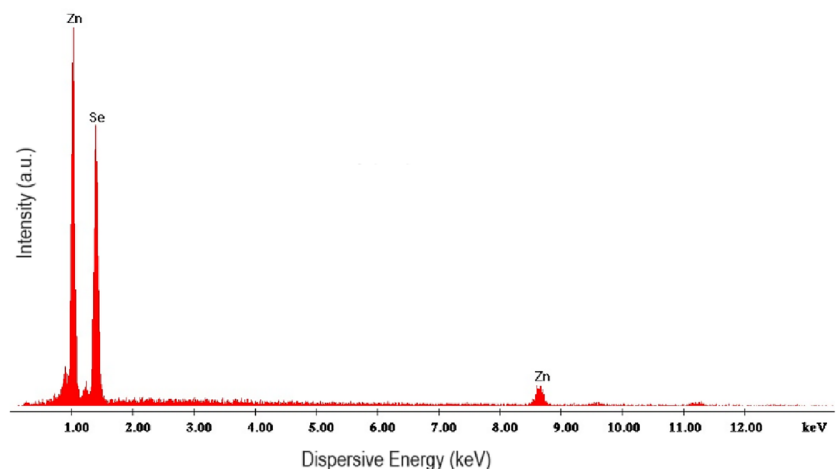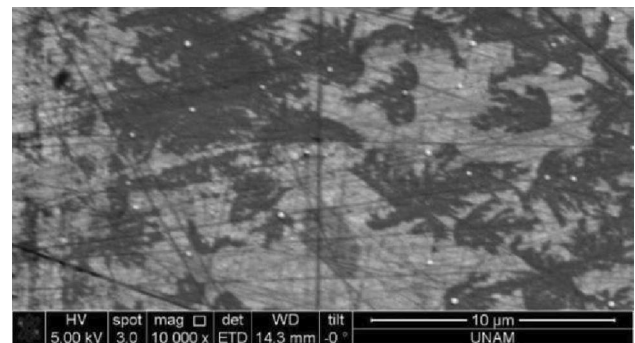
2.2 Plasma measurements

Figure 8 shows schematic representation of the gas discharge-semiconductor microplasma system (GDSS) cell module equipped with charge-coupled device (CCD) [43] for recording plasma patterns in UV–Vis wavelength ranges in the Plasma Research Laboratory. On the infrared-illuminated side of photocathode, gold (Au) thin film with a thickness of 40 nm was deposited on zinc selenide (ZnSe) wafer as NIR-transparent electrical contact. On the visible-irradiation side of anode, indium tin oxide (ITO) film with a thickness of 80 nm was grown on fused-silica substrate [44] as VIS-transparent electrical contact.

Current-Voltage Characteristics (CVCs) were examined to exhibit the infrared sensitivity of ZnSe cathode sample in Ar gas medium charged at 5.86 kPa (44 Torr) subatmospheric pressure. After breakdown voltage, current showed instantenous increase depending on the infrared illumination intensity as a function of
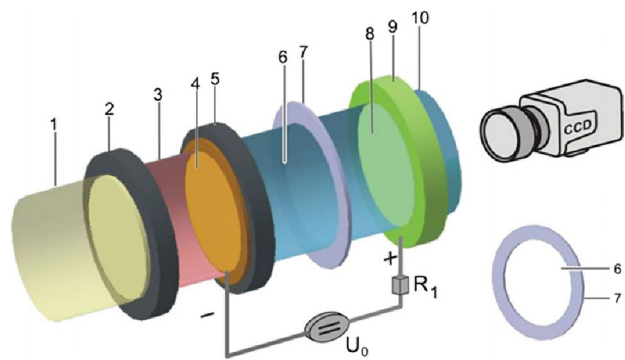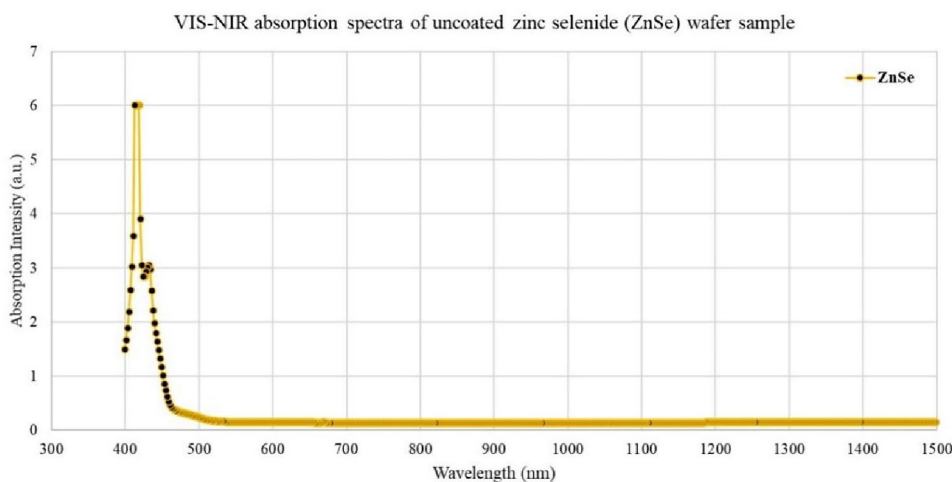

Fig. 5 Surface image of ZnSe sample taken at 10,000X magnification by SEM.

Fig. 4 EDAX data of ZnSe sample with 65.04% Se and 34.96% Zn elements by weight

Fig. 6 AFM surface images of ZnSe sample with a scan area of 1 μm × 1 μm: **a** 2D planar surface image, **b** 3D topographic image
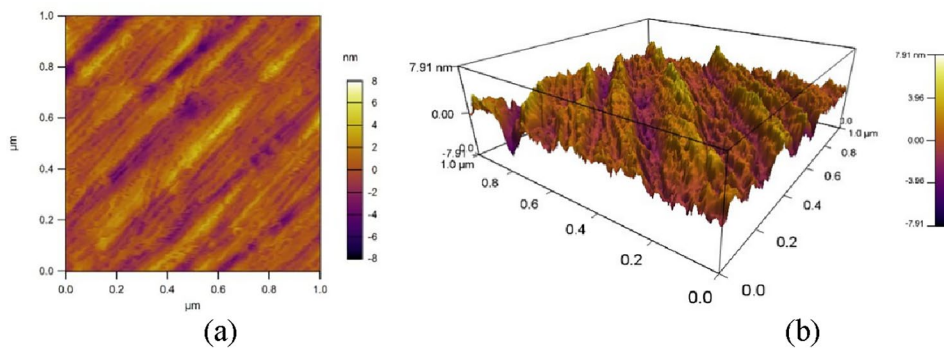
Fig. 7 VIS–NIR absorption spectra of uncoated ZnSe sample


Fig. 8 Schematic of GDSS cell module equipped with CCD for performing the IR-VIS wavelength conversion experimental studies: **1** light source, **2** Silicon filter, **3** IR beam input, **4** IR transparent thin Au contact, **5** ZnSe photo-cathode disc, **6** Discharge micro gap, **7** Mica dielectric separator, **8** VIS beam output, **9** VIS transparent thin ITO [44] contact, **10** Fused silica

voltage as shown in Fig. 9. Dielectric breakdown is one of the most important state which is driven by the mutual balance between the production of charged particles and their losses in the recombination and diffusion processes across plasma cell. As it can be seen from the CVCs, infrared illumination intensity has a significant effect on the breakdown voltage. The breakdown was around 600 V under strong illumination intensity, while it was around 700 V under weak illumination intensity.

When the gas discharge-semiconductor cell was illuminated with infrared light beam, various types of micro discharges were observed. The experimental measurements of the glow discharge light emissions (GDLE) were carried out by setting the pressures at 100 Torr and 760 Torr to investigate the pressure effect on the plasma radiation. While the gas medium was insulating until the dielectric breakdown point was reached, the transition from non-conductive state to conductive state of gas medium occured by increasing the illumination intensity on ZnSe cathode as shown in Fig. 10a, b.
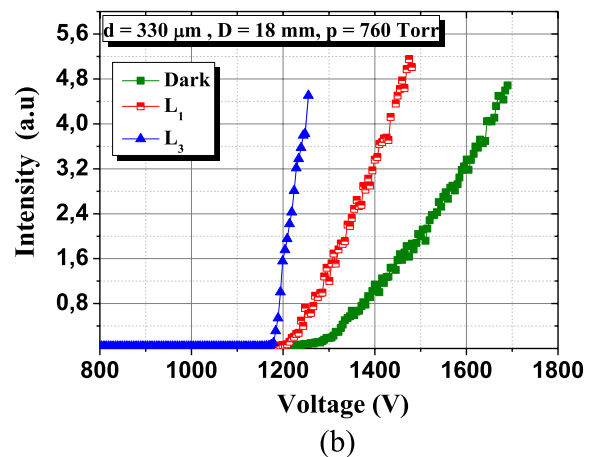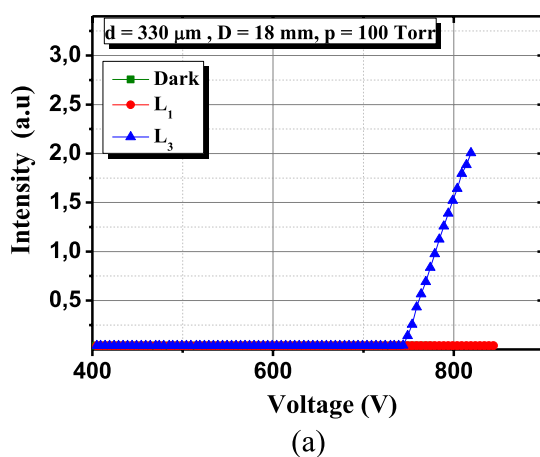
The peak plasma radiation intensity of 5.2 (a.u.) was obtained at 760 Torr atmospheric pressure under strong (L_3) level of infrared illumination. The impact
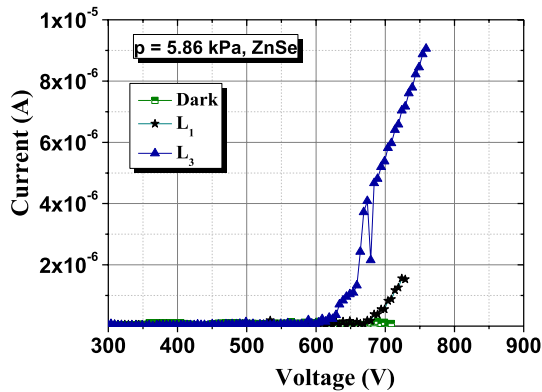
Fig. 9 Current (I)–Voltage (V) graphs under three different intensities of infrared (IR) illumination at dark, weak (L_1), and strong (L_3) levels for the experimental GDSS cell. ZnSe -coupled microgap was charged with Ar gas at 5.86 kPa (44 Torr) subatmospheric pressure

ionization effect, which causes an increase in the number of electrons, has been found to play an important role in the field emission at microscale discharge gaps.

In this study, simulation studies were carried out to investigate the fast transient discharge behaviours of gas discharge-semiconductor microplasma systems that we can not observe experimentally. Binary Ar/H_2 gas discharge model was numerically analyzed in terms of key discharge parameters and compared with the basic unary Ar gas discharge model. Two comparative models were run to exhibit the respective

transient glow discharge properties of GDSµPS cell from electron field emission state to self-sustained normal glow discharge state by numerically solving the electron density (ED), electron current density (ECD) and electric potential distribution (EPD) parameters using the finite-element method (FEM) solver COMSOL Multiphysics DC plasma program. Numerical analyses were performed based on mixture-averaged diffusion drift theory and Maxwellian electron energy distribution function.

Figure 11 shows physical layout of two-dimensional planar GDSµPS simulation model.

The simulation model of GDSµPS cell is defined with the following parameters:

i. Stationary power source to drive and sustain microplasma: V = 1.0 kV DC.
ii. Plasma process medium: Argon (Ar) mixed with hydrogen (H_2) at 3:2 molar ratio.
iii. Process gas pressure: P = 200 Torr.
iv. Ambient cell operating temperature: T = 300 K.
v. Gas discharge gap distance (Anode-to-Cathode): d = 50 µm.
vi. Cathode electrode: Zinc selenide (ZnSe) semiconductor.
vii. Infrared-illuminated side of ZnSe photocathode: 40 nm thick gold (Au) film.
viii. Cathode electron emission surface: Digitated in comb plate style.
ix. Cathode electrode radius: r = 50 µm.

Fig. 10 Plasma radiation curves under three different intensities of infrared (IR) illumination at dark, weak (L_1), and strong (L_3) l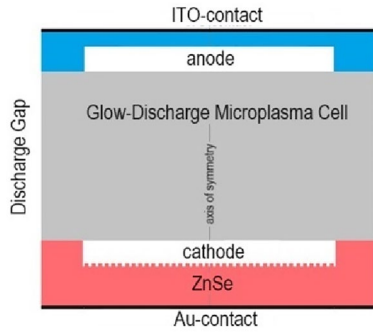evels for the experimental GDSS cell. ZnSe -coupled microgap was respectively charged with Ar gas at pressures of: **a** 100 Torr, **b** 760 Torr. D: cathode diameter, d: discharge gap
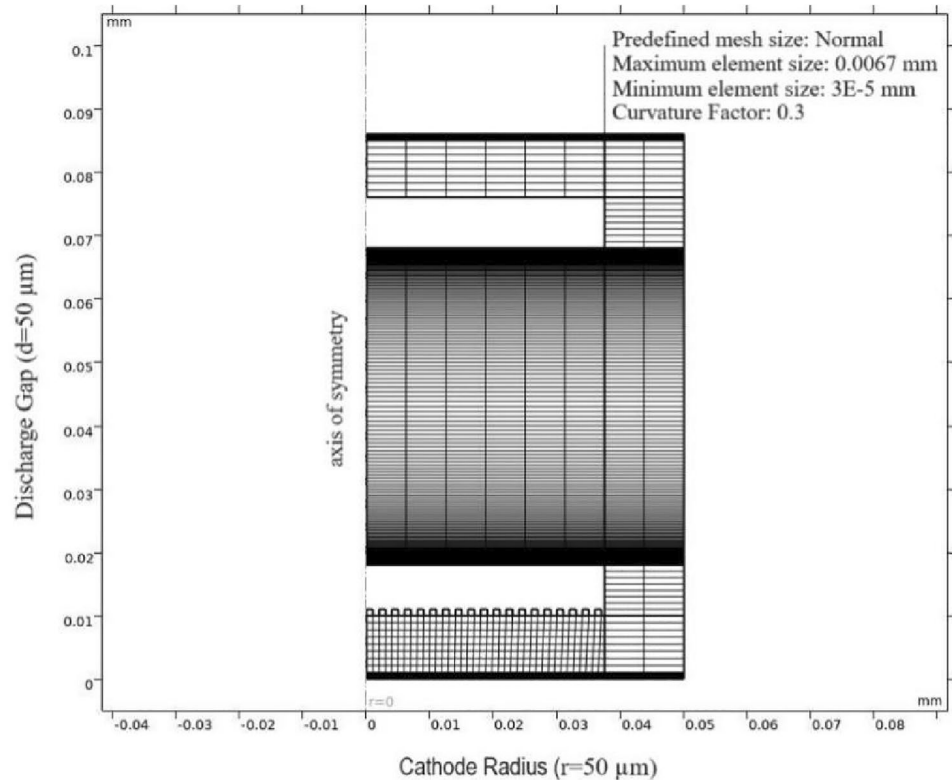
Fig. 11 Physical layout of the proposed 2D-planar GDSµPS simulation model

  x.   Anode electrode: Fused-silica substrate with indium tin oxide (ITO) contact.

  xi.   Initial electron density in the plasma reactor cell: $n_{e,o} = 1.0 \times 10^{17}$ (1/m³).

  xii.   The calculated operating line on Paschen curve: P.d = 200 Torr.50 µm = 1.0 Torr.cm.

Figure 12 shows the boundary-seperated mesh structure used in the two-dimensional simulation model for the proposed GDSµPS cell.

Mesh size parameters including, number of elements predefined in the cell structure, mesh area, maximum element size and minimum element size values were tabulated in Table 1.

Figure 13 shows the simulation results for Electron Density (ED) parameter across planar 50 µm gap in unary Ar and binary Ar/H$_2$ (3:2) gas discharge media coupled to ZnSe cathode; (a, b) 1D-ED plots of complete plasma-process period, (c, d) 2D-ED surface images of final plasma-process phase, (e, f) 3D-ED solid images of final plasma-process phase, respectively

Figure 14 shows the simulation results for Electron Current Density (ECD) parameter across planar 50 µm

Table 1 Predefined mesh size parameters used in the simulation model

Description	Value
Number of elements	2019
Mesh area	0.003719 mm²
Maximum element size	0.0067
Minimum element size	3E-5

Fig. 12 Mesh structure of two-dimensional simulation model for GDSµPS cell

(a)

(b)

(c)

(d)

(e)

(f)
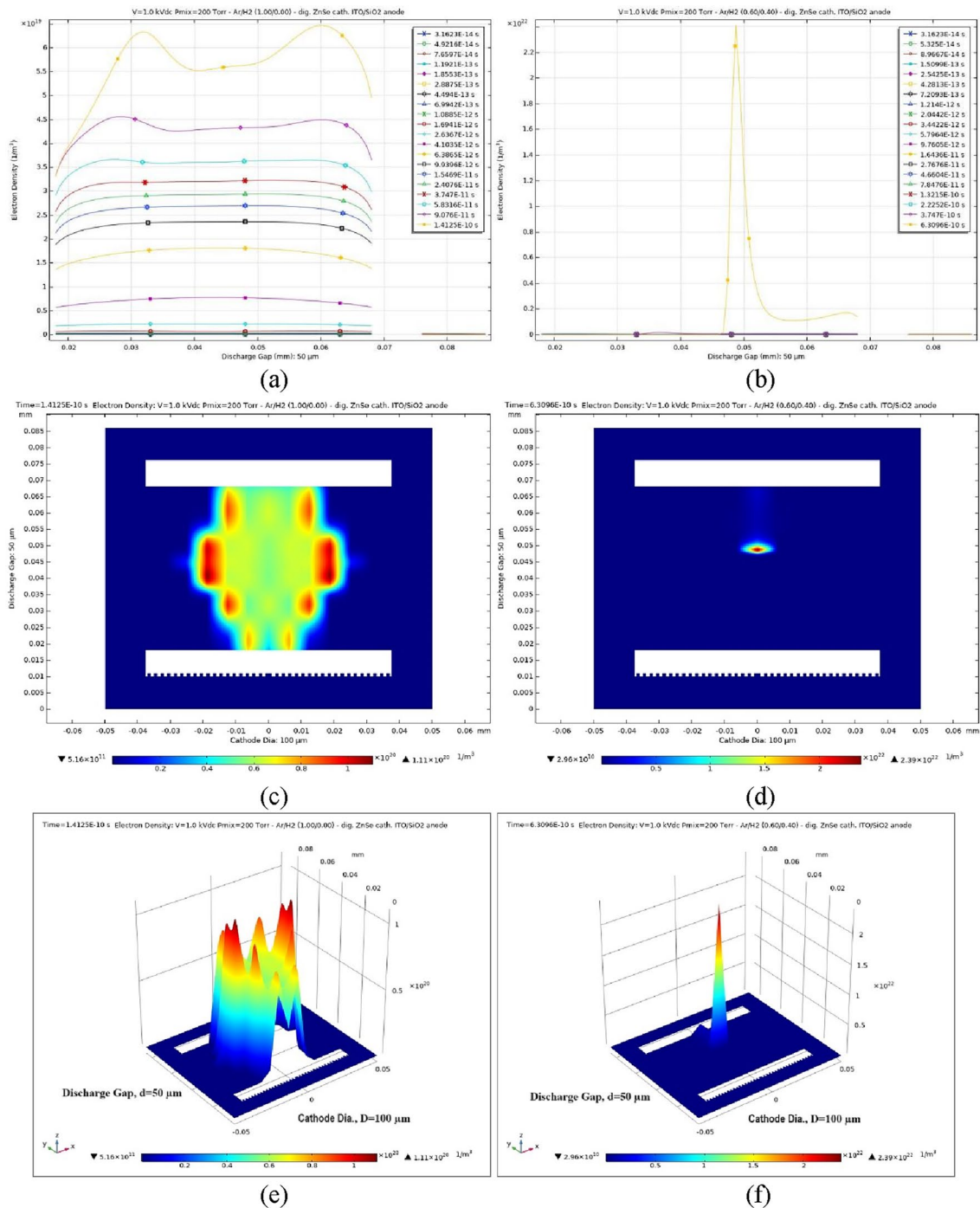
Fig. 13 Simulation results for Electron Density (ED) parameter across planar 50 μm gap in unary Ar and binary Ar/H 2 (3:2) gas discharge media coupled to ZnSe cathode: **a** 1D-ED plots of complete plasma-process period for unary Ar micro-discharges. **b** 1D-ED plots of complete plasma-process period for binary Ar/H 2 micro-discharges. **c** 2D-ED surface image of final plasma-process phase for unary Ar micro-discharges. **d** 2D-ED surface image of final plasma-process phase for binary Ar/H 2 micro-discharges. **e** 3D-ED solid image of final plasma-process phase for unary Ar micro-discharges. **f** 3D-ED solid image of final plasma-process phase for binary Ar/H 2 micro-discharges
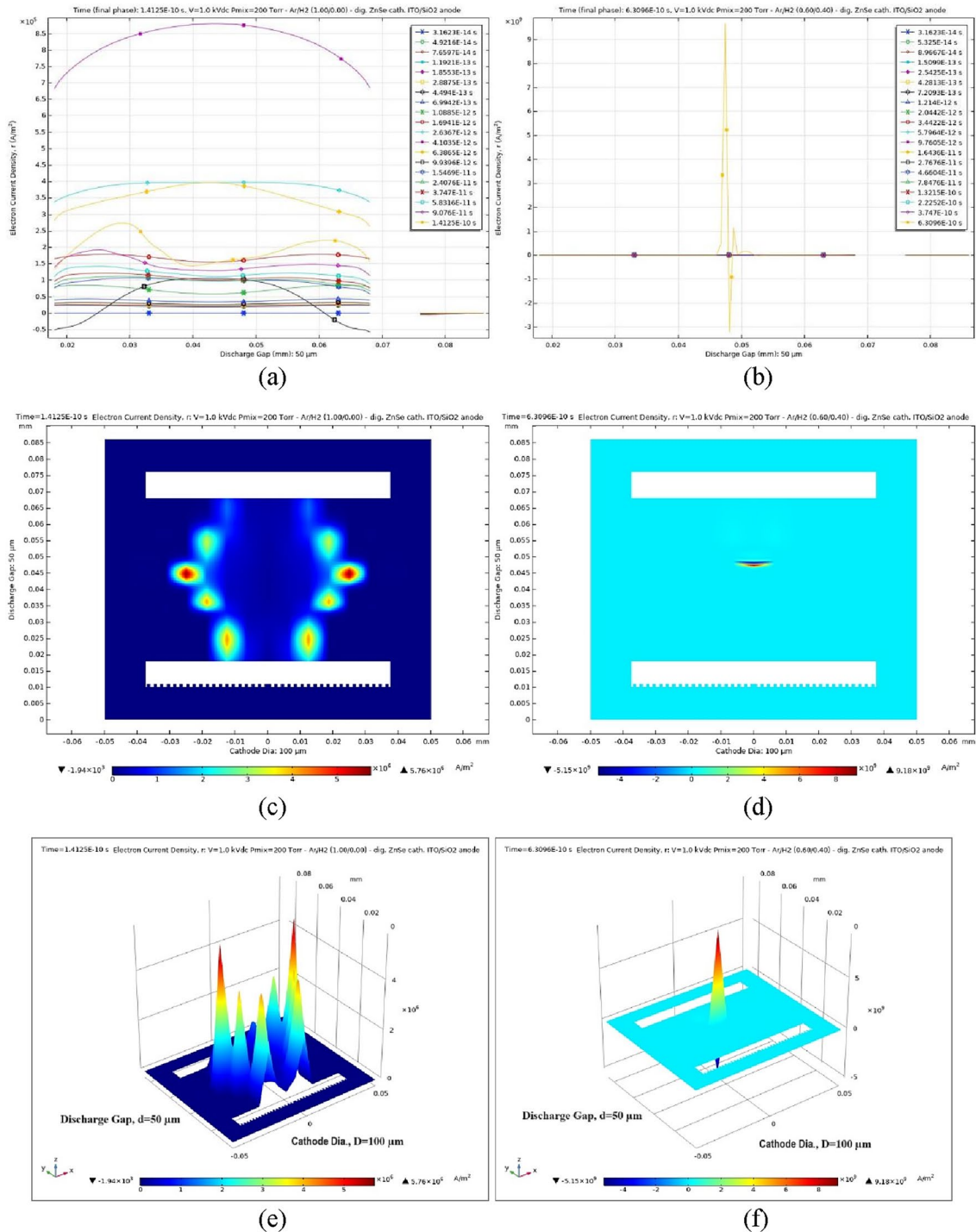
Fig. 14 Simulation results for Electron Current Density (ECD) parameter across planar 50 μm gap in unary Ar and binary Ar/H 2 (3:2) gas discharge media coupled to ZnSe cathode: **a** 1D-ECD plots of complete plasma-process period for unary Ar micro-discharges. **b** 1D-ECD plots of complete plasma-process period for binary Ar/H 2 micro-discharg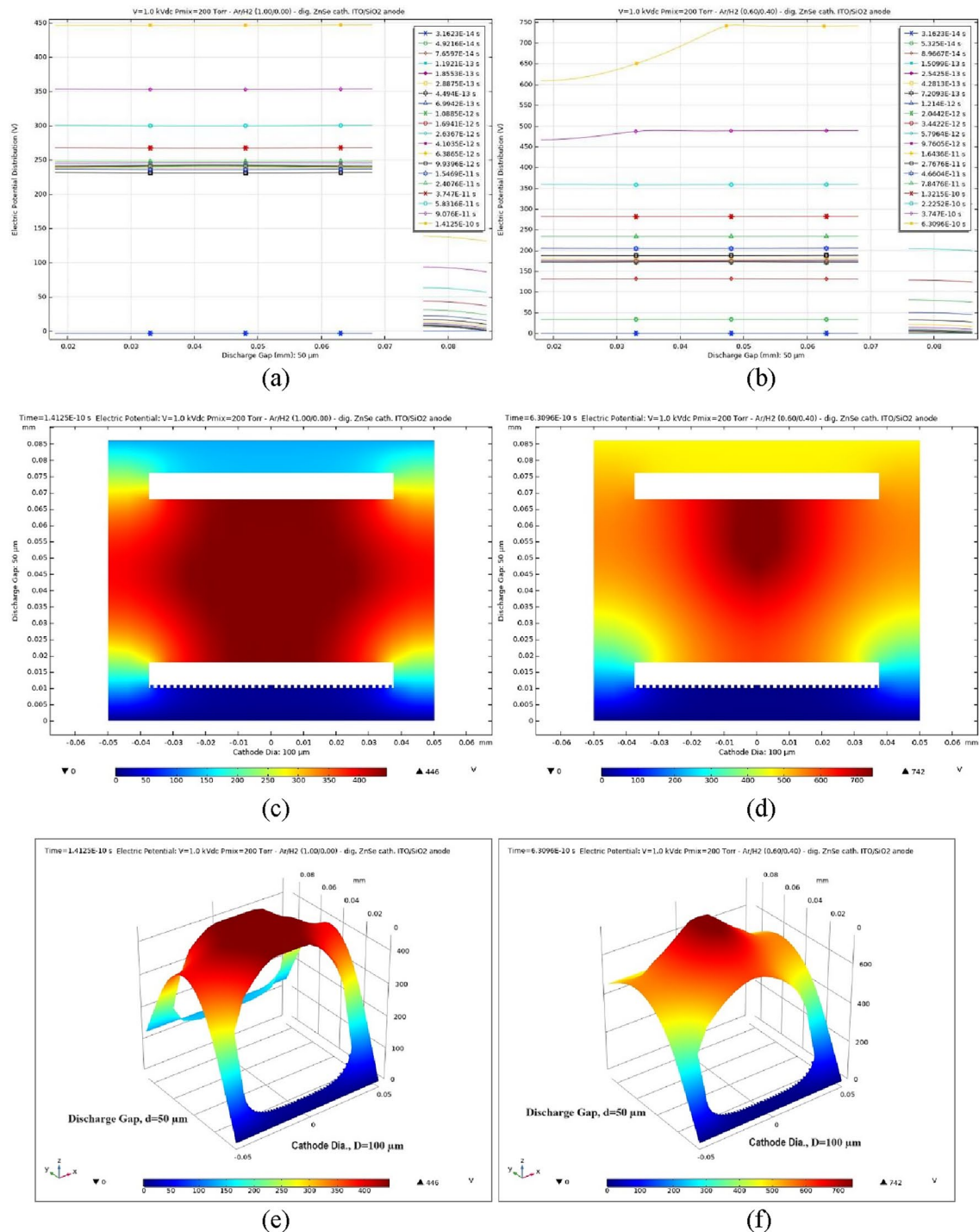es. **c** 2D-ECD surface image of final plasma-process phase for unary Ar micro-discharges. **d** 2D-ECD surface image of final plasma-process phase for binary Ar/H 2 micro-discharges. **e** 3D-ECD solid image of final plasma-process phase for unary Ar micro-discharges. **f** 3D-ECD solid image of final plasma-process phase for binary Ar/H 2 micro-discharges
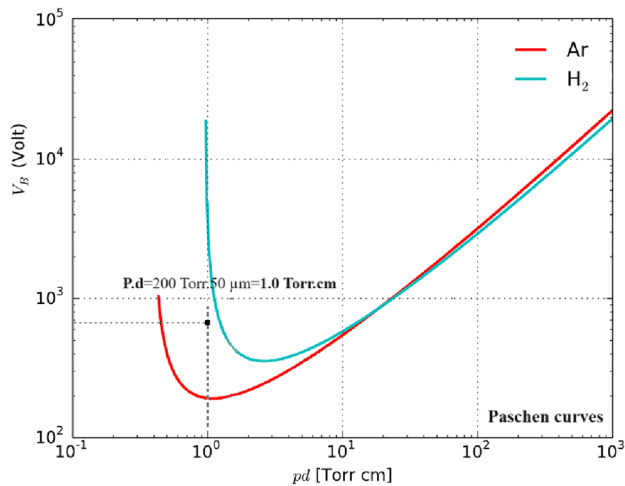
Fig. 15 Simulation results for Electric Potential Distribution (EPD) parameter across planar 50 µm gap in unary Ar and binary Ar/H $_2$ (3:2) gas discharge media coupled to ZnSe cathode: **a** 1D-EPD plots of complete plasma-process period for unary Ar micro-discharges. **b** 1D- EPD plots of complete plasma-process period for binary Ar/H $_2$ micro-discharges. **c** 2D- EPD surface image of final plasma-process phase for unary Ar micro-discharges. **d** 2D- EPD surface image of final plasma-process phase for binary Ar/H $_2$ micro-discharges. **e** 3D- EPD solid image of final plasma-process phase for unary Ar micro-discharges. **f** 3D-EPD solid image of final plasma-process phase for binary Ar/H $_2$ micro-discharges

Table 2 Electron Density (ED), Electron Current Density (ECD) and Electric Potential Distribution (EPD) data as per calculated at the final phase of the plasma process period

Basic Unary Gas Model Ar	Advanced Binary Gas Model Ar/H$_2$ (3:2)
Final plasma-process phase, output time (s)	
1.4125×10^{-10}	6.3096×10^{-10}
Electron Density, peak_ED (1/m^3)	
1.11×10^{20}	2.39×10^{22}
Electron Current Density, peak_ECD (A/m^2)	
5.76×10^6	9.18×10^9
Electric Potential, peak EPD (V)	
446	742

Fig. 16 The approximated operating point of the proposed GDSμPS cell model is indicated below V$_B$ by the square dot in the space between Paschen curves of Ar and H$_2$ gases [6], located on the imaginary vertical projection line corresponding to P.d = 1.0 Torr.cm by this study

gap in unary Ar and binary Ar/H$_2$ (3:2) gas discharge media coupled to ZnSe cathode; (a-b) 1D- ECD plots of complete plasma-process period, (c-d) 2D- ECD surface images of final plasma-process phase, (e-f) 3D- ECD solid images of final plasma-process phase, respectively.

Figure 15 shows the simulation results for Electric Potential Distribution (EPD) parameter across planar 50 μm gap in unary Ar and binary Ar/H$_2$ (3:2) gas discharge media coupled to ZnSe cathode; (a-b) 1D-EPD plots of complete plasma-process period, (c-d)

2D- EPD surface images of final plasma-process phase, (e-f) 3D- EPD solid images of final plasma-process phase, respectively.

Referring to the simulation results of Electron Density (ED) parameter in Fig. 13b–d–f), the proposed GDSμPS cell model with binary Ar/H$_2$ (3:2) gas discharge medium -coupled to ZnSe cathode, exhibits a characteristic spatiotemporal ED pattern closest to the Maxwellian shape with more localized and higher intensity at the final phase of plasma process period as calculated with reference to the basic cell model with unary Ar gas discharge medium.

Electron Density (ED), Electron Current Density (ECD) and Electric Potential Distribution (EPD) data, measured at the respective final plasma process phases, were tabulated in Table 2.

Figure 16 exhibits the Paschen curves for argon and hydrogen gases [6]. It is aimed to locate and tune the operating point of GDSμPS cell on the imaginary vertical projection line corresponding to P.d = 200 Torr.50 μm = 1.0 Torr.cm by this study. Thus, the approximated operating point of the proposed GDSμPS cell model is defined below critical breakdown voltage (V$_B$) as indicated by the square dot in the space between Paschen curves of Ar and H$_2$ gases.

The peak discharge current at final plasma-process phase is increased from around 0.5 up to 10 mA according to the calculated ECD data of unary and binary gas models, respectively, as per given in Table 2. The virtual operating points of unary and binary gas models were indicated in the normal glow discharge regime of the I–V curve in Fig. 17.

3 Conclusion

This work is dedicated to a comprehensive understanding of the fundamental processes involved in plasma and related applications experimentally and theoritically. For this purpose, experimental data, obtained from both structural and elemental analyses (EDAX, SEM, AFM and UV–Visible) and also plasma interactions of ZnSe, were presented comprehensively. It is revealed that the plasma emits maximum radiation (i.e. 5.2 (a.u)) under specific discharge conditions ($p = 760$ Torr) covering the entire ZnSe cathode surface. Further, the spatio-temporal microplasma patterns were determined by simulation method theoretically.

Fig. 17 The characteristic I–V curve of gas discharge system [6]. The virtual operating points of unary and binary gas models were indicated in the normal glow discharge regime
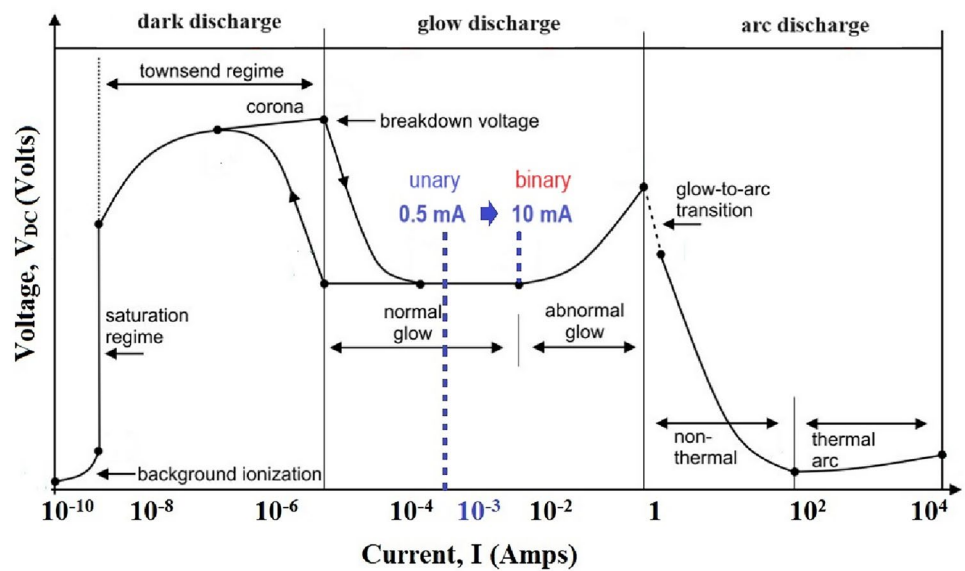
When theoretically-found plasma patterns were examined, it was understood that electron-impact excitation/ionization effects were decisive.

It is figured out that binary Ar/H_2 gas discharge model can undertake a major role in shaping and controlling the spatiotemporal response to transient electro-optical behavior of microplasma-based artificial electromagnetic materials configured for high-efficiency infrared-to-visible wavelength conversion applications.

The optimum operating point of GDSμPS cell can be tuned on the Paschen curve by means of hydrogen addition to argon. Binary Ar/H_2 (3:2) gas discharge model exhibited the characteristic electron density (ED) distribution close to the Maxwellian shape with highly localized electron gas as calculated at the final phase of plasma process period.

The virtual operating point of binary gas model is shifted rightwards in the normal glow discharge regime of the I-V curve from around 0.5 to 10 mA of peak discharge current rating as calculated based on the electron current density (ECD) at the final plasma-process phase.

We suppose that by means of hydrogen addition to argon when mixed in a proper fraction; key features including, infrared sensitivity, response speed, NIR-VIS conversion efficiency of the GDSS cell could be enhanced. Thus, low-energy and small numbers of photons of near-infrared light can be directly detected and efficiently converted into high-energy and large numbers of photons of visible light by a GDSS device designed according to the application requirements.

Authors contributions

EO: Modeling, simulation, article writing. SU: Simulation. HHY: Expert in theoretical and experimental plasma physics, modeling, simulation, article writing and editing.

Data availability

The data that support the findings of this study are available on request from the corresponding author.

Declarations

Conflict of interest　The authors declare no conflict of interest in this study.

Ethical standards　The authors declare that the materials and methods used in this study do not require ethical committee permission and/or legal-special permission.

References

1. J.L. Vossen, Thin Film Processes, *Academic Press, INC., New York* (1978)
2. H.Y. Kurt, E. Kurt, B.G. Salamov, Fractal processing for an analysis of the quality and resistivity of large semiconductor plates. Cryst. Res. Technol. **39**(9), 743–753 (2004)
3. D.B. Go, A. Venkattraman, Microscale gas breakdown: Ion-enhanced field emission and the modified Paschen's curve. J. Phys. D Appl. Phys. **47**, 503001 (2014)
4. L. Liangliang, Q. Wang, Microplasma, A New Generation of Technology for Functional Nanomaterial Synthesis. Plasma Chem. Plasma Process. **35**, 925–962 (2015)
5. K.H. Schoenbach, K. Becker, 20 years of microplasma research: a status report. Eur. Phys. J. D **70**, 29 (2016)
6. M. Tabib-Azar, P. Pai, Microplasma Field Effect Transistors Micromachines. **8**, 117 (2017)
7. A.L. Garner, G. Meng, Y. Fu et al., Transitions between electron emission and gas breakdown mechanisms across length and pressure scales. J. Appl. Phys. **128**, 210903 (2020)
8. A.L. Garner, A.M. Loveless, J.N. Dahal, A. Venkattraman, A tutorial on theoretical and computational techniques for gas breakdown in microscale gaps. IEEE Trans. Plasma Sci. **48**, 808–824 (2020)
9. W.-H. Chiang, D. Mariotti, R.M. Sankaran, J.G. Eden, K. Ostrikov, Microplasmas for advanced materials and devices. Adv. Mater. **32**, 1905508 (2020)
10. E. Tournié et al., Mid-infrared III–V semiconductor lasers epitaxially grown on Si substrates. Sci. Appl. **11**, 165 (2022)
11. Q. Wang, D.J. Economou, V.M. Donnelly, Simulation of a direct current microplasma discharge in Helium at atmospheric pressure. J. Appl. Phys. **100**, 023301 (2006)
12. M.M. Bülbül, H.H. Kurt, B. Salamov, Surface behaviour of plasma etched photodetector in a planar gas discharge image converter, Malmö, Sweden. *7th Int'l Conference on Nanometer-Scale Science and Technology (ECOSS-21)* (2002)
13. H.Y. Kurt, B.G. Salamov, T.S. Mammadov, Electrical instability in a semiconductor gas discharge system. Cryst. Res. Technol. **40**(12), 1160–1164 (2005)
14. H.Y. Kurt, Y. Sadiq, B.G. Salamov, Nonlinear electrical characteristics of semi-insulating GaAs. Phys. Status Solidi (a). **205**(2), 321–329 (2008)
15. Y. Sadiq, H.Y. Kurt, A.O. Albarzanji, S.D. Alekperov, B.G. Salamov, Transport properties in semiconductor-gas discharge electronic devices. Solid State Electron. **53**(9), 509–1015 (2009)
16. H.Y. Kurt, A. Inalöz, B.G. Salamov, Study of non-thermal plasma discharge in semiconductor gas discharge electronic devices. Optoelectron. Adv. Materials-Rapid Commun. **4**, 205 (2010)
17. H.H. Kurt, E. Koc, B.G. Salamov, Atmospheric pressure DC Glow Discharge in Semiconductor Gas Discharge Electronic devices. IEEE Trans. Plasma Sci. **38**(2), 137–141 (2010)
18. H.Y. Kurt, G. Kalkan, M. Özer, E. Tanrıverdi, The Effect of the oxidation on GaAs Semiconductor Surface to the system characteristics in a double-gapped plasma cell. J. Polytechnic. **17**(4), 161–165 (2014)

19. H.H. Kurt, E. Tanrıverdi, The features of GaAs and GaP Semiconductor cathodes in an Infrared Converter System. J. Electron. Mater. **46**, 4024–4033 (2017)

20. H.H. Kurt, E. Tanrıverdi, Electrical properties of ZnS and ZnSe semiconductors in a plasma-semiconductor system. J. Electron. Mater. **46**, 3965 (2017)

21. H.H. Kurt, B.G. Salamov, Breakdown Phenomenon and Electrical Process in a Microplasma System with InP Electrode, *7th European Conference on Renewable Energy Systems*, JOM 72, 651–657 (2020)

22. E. Ongun, S. Utaş, H.H. Yücel, A. Hançerlioğulları (eds.), The investigation of spatiotemporal dynamics of planar DC field emission-driven gas discharge-semiconductor microplasma system (GDSμPS), *Turkish Physical Society 39th International Physics Congress*, 31 August-04 September 2023, Bodrum Türkiye

23. A. Rogalski, Recent progress in infrared detector technologies. Infrared Phys. Technol. **54**(3), 136–154 (2011)

24. P.R. Norton, Infrared detectors in the next millennium, *Proc. SPIE* 3698, 652 (1999)

25. F. Niklaus, C. Vieider, H. Jakobsen, MEMS-based uncooled infrared bolometer arrays: a review, *Photonics Asia 2007*, pp. 68360D-15 (2007)

26. L. Plucinski, R.L. Johnson, A. Fleszar, W. Hanke, W. Weigand, C. Kumpf, E. Hesks, T. Umbach, L. Schallenberg, W. Molenkamp, Phys. Rev. B **70**, 1 (2004)

27. M.C. Beard, G.M. Turner, C.A. Schmuttenmaer, Nano Lett. **2**, 983 (2002)

28. X.S. Fang, T.Y. Zhai, U.K. Gautam, L. Li, L. Wu, Y. Bando, D. Golberg, Prog Mater. Sci. **56**, 175 (2011)

29. R.B. Kale, C.D. Lokhande, Appl. Surf. Sci. **252**, 929 (2005)

30. G.M. Lohar, R.K. Kamble, S.T. Punde, S.T. Jadhav, A.S. Dhaygude, H.D. Relekar, B.P. Fulari, Mater. Focus. **5**, 481 (2016)

31. P. Dinesh, S. Kuldeep, N.S. Rathore, S. Saxena Kananbala, T.P. Sharma, Jr Mod. Opt. **55**, 3041 (2008)

32. H.N. Desai, J.M. Dhimmar, B.P. Modi, Int. Jr Eng. Res. Appl. **5**, 2248 (2015)

33. D.A. Buba, Br. J. Appl. Sci. Technol. **14**, 1 (2016)

34. K. Umesh, B. Sulakshana, P. Panjabrao, Mater. Sci. Appl. **3**, 36 (2012)

35. J.C. Banthí-Barcenas, F. Sutara, I. Hernández-Calderón, Design of a quantum well based on a ZnCdSe/ZnTe type II heterostructure confined type I within ZnSe barriers, 8th International Conference on Low Dimensional Structures and Devices (LDSD 2016), *AIP Conf. Proc* 1934, 030001 (2018)

36. B.H. Amrollahi, M.B. Zarandi, Mater. Chem. Phys. **5**, 1 (2011)

37. C.D. Aparna, B.S. Shashi, A. Majid Kazemian, P. Renu, S.K. Kulkarni, Mater. Lett. **62**, 3803 (2008)

38. C.I. Nweze, A.J. Ekpunobi, Int. Jr Sci. Technol. Res. **3**, 201 (2014)

39. B.H. Morkoc, S. Strite, G.B. Gao, M.E. Lin, B. Sverdlov, M. Burns, Large-band-gap SiC, III-V nitride, and II-VI ZnSe-based semiconductor device technologies. J. Appl. Phys. **76**(3), 1363–1398 (1994)

40. L. Yan, J.A. Woollam, E. Franke, Oxygen plasma effects on optical properties of ZnSe films. J. Vacuum Sci. Technol. A: Vacuum Surf. Films. **20**(3), 693–701 (2002)

41. H.H. Kurt, Exploration of the infrared sensitivity for a ZnSe electrode of an IR image converter. J. Electron. Mater. **47**(8), 4486–4492 (2018)

42. P.Y. Yu, M. Cardona, Fundamentals of Semiconductors: Physics and Materials Properties, *Graduate Texts in Physics, Fourth Edition, Springer* (2010)

43. H.H. Kurt, Exploration of gas discharges with GaAs, GaP and ZnSe electrodes under Atmospheric pressure. J. Electron. Mater. (2018). https://doi.org/10.1007/s11664-018-6161-5

44. M. Alaa, Abd-Elnaiem, A. Hakamy, Influence of annealing temperature on structural, electrical, and optical properties of 80 nm thick indium doped tin oxide on borofloat glass. J. Mater. Sci: Mater. Electron. **33**, 23293–23305 (2022). https://doi.org/10.1007/s10854-022-09051-6